Compound Flooding in Convergent Estuaries:
Insights from an Analytical Model

5   Ramin Familkhalili[1], Stefan A. Talke[2], and David A. Jay[3]

6   [1]Department of Civil and Environmental Engineering, Old Dominion University, Norfolk, VA, USA

7   [2]Department of Civil and Environmental Engineering, California Polytechnic State University, San Luis Obispo, CA, USA

8   [3]Department of Civil and Environmental Engineering, Portland State University, Portland, OR, USA

14   *Correspondence to*: Ramin Familkhalili (rfamilkh@odu.edu)

Key Points

- An idealized analytical model shows that deepening an estuarine channel reduces the impacts of river flow on peak water level but increases the effects of storm tide.
- A friction number shows the competing effects of surge time scale, depth, and convergence on water level amplitudes.
- Channel deepening changes the balance of fluvial and coastal flood risks and moves the crossover between storm tide vs. fluvial-dominated flooding landward.

Abstract

We investigate here the effects of geometric properties (channel depth and cross-sectional convergence length), storm surge characteristics, friction, and river flow on the spatial and temporal variability of compound flooding along an idealized, meso-tidal coastal-plain estuary. An analytical model is developed that includes exponentially convergent geometry, tidal forcing, constant river flow, and a representation of storm surge as a combination of two sinusoidal waves. Non-linear bed friction is treated using Chebyshev polynomials and trigonometric functions, and a multi-segment approach is used to increase accuracy. Model results show that river discharge increases the damping of surge amplitudes in an estuary, while increasing channel depth has the opposite effect. Sensitivity studies indicate that the impact of river flow on peak water level decreases as channel depth increases, while the influence of tide and surge increases in the landward portion of an estuary. Moreover, model results show less surge damping in deeper configurations and even amplification in some cases, while increased convergence length scale damps surge waves with time scales of 12 h-72 h along an estuary. For every modeled scenario, there is a point where river discharge effects on water level outweigh tide/surge effects. As a channel is deepened, this cross-over point moves progressively upstream. Thus, channel deepening may alter flood risk spatially along an estuary and reduce the length of a river-estuary, within which fluvial flooding is dominant.

Plain language summary

Storm surge, tides, and high river flow often combine to cause flooding in estuaries. In this study we investigate these factors and how changes to estuary and river geometry influence peak water levels. Our results show that surge waves become larger when the depth of a shipping channel is increased, for example due to dredging or sea-level rise. The same deepening, however, reduces the effect of river flow on peak water level. The result is that the region over which river influence dominates the peak water level moves upstream as a system becomes deeper. This change in the 'cross-over location' reduces the domain over which river flooding is the dominant consideration. This study offers an analytical framework for reducing river-estuary flood risk by better

58   understanding of how bathymetry, surge time scale, and river discharge affect surge and tidal
59   amplitudes, and therefore flood heights and inundation, in these systems.

60   Keywords: Analytical model, Compound flooding, Estuary, Surge, Tide

1- Introduction

62   Many low-lying coastal and riverine areas have been affected by combined coastal and riverine
63   floods over the last few decades (e.g., Jongman et al., 2012; Nicholls et al., 2007). In cases such
64   as Hurricane Harvey (Gulf of Mexico, August 2017), flooding was driven primarily by
65   precipitation and runoff (e.g., van Oldenborgh et al., 2017; Wang et al., 2018). Other flood events,
66   e.g., Hurricane Sandy, were forced by the combined effects of tide and storm surge (i.e., by storm
67   tides; Orton et al., 2016). Some storm events (such as Hurricanes Irene and Irma) produce both
68   coastal and inland flooding because both storm surge and river flow produce elevated coastal water
69   levels in a spatially varying pattern (e.g., Orton et al., 2012; Ralston et al., 2013; Talke et al., 2021).
70   Collectively, a flooding event that is influenced by both storm tide and precipitation run-off is
71   known as a 'compound flood' (e.g., Zscheischler et al., 2018; Wahl et al., 2015). The relative
72   timing of the coastal and fluvial forcing, and the time scale over which water levels are elevated,
73   matters in terms of impact (e.g., Zheng et al., 2014). Storm surge flooding generally occurs first
74   and for a shorter period (i.e., time scales of hours to a day or two) than river flooding, which may
75   last for weeks or even months, particularly in regions with a large watershed and flat topography
76   (e.g., Johnson et al., 2016, Wong et al., 2014). The timing of storm surge relative to tidal high-
77   water (Familkhalili and Talke, 2016) or the spring-neap tidal cycle influences flood heights, even
78   upstream of tidal influence (Helaire et al., 2020). Therefore, understanding tidal, surge and river
79   flow dynamics, and how they combine and interact to produce the maximum or total water level
80   (TWL), has obvious implications for emergency planning.

81   The spatial variability of compound flooding is influenced by the geometry of an estuary region
82   and may change over time due to system alterations, including channel deepening, sea-level rise,
83   and wetland reclamation (Ralston et al., 2019; Helaire et al., 2019, 2020). Recent studies have
84   shown that human-caused changes to the geometry of estuaries affects the dynamics of long-waves
85   (see reviews by Talke and Jay, 2020, and Jay et al., 2021), with tidal range in some regions more
86   than doubling (e.g., Winterwerp et al., 2013). Similar effects are observed with storm surge; for
87   example, doubling the depth of the shipping channel in the Cape Fear Estuary was modeled to
88   increase the magnitude of a worst-case scenario storm surge in Wilmington (NC) by 3.8 ± 0.25 m
89   to 5.6 ± 0.6 m (Familkhalili and Talke, 2016). By contrast, depth increases often cause the mean
90   water level in tidal rivers to drop, due to decreased frictional effects (Jay et al., 2011; Helaire et
91   al., 2019); hence, flood risk in Albany (NY) has significantly dropped over the past 150 years,
92   despite a doubling of tide range and an increase in storm surge magnitudes (Ralston et al., 2019).
93   Closer to the coast, flood hazard within the same estuary markedly increased over the same time

94   period (e.g., Talke et al., 2014). Hence, non-stationarity in flood hazard can be spatially variable,
95   to an extent that is just beginning to be quantified.

96   In this contribution, we study the relative influence of river flow and storm surge effects along the
97   river-estuary continuum from a dynamical perspective that enables us to assess the effects of non-
98   linear interactions, geometry, and changing (non-stationary) conditions. An idealized approach is
99   used, which enables a large parameter space to be assessed and the following two dynamical
100   questions to be investigated:

101   a) What factors determine the region in which river flow effects or tide/surge effects dominate
102   the total water level?
103   b) How does the transition from coastal to fluvial dominance shift as geometry changes or as
104   properties of storm surge (e.g., time scale and magnitude) and river flow (magnitude)
105   change?

106   We combine a three-sinusoidal wave analytical model based on Jay (1991) with the multi-wave
107   and multi-segment approach of Giese and Jay (1989) (see Familkhalili et al., (2020) for details) to
108   quickly query a parameter space or relevant factors and provide insight into how factors such as
109   storm time scale and the relative magnitudes of different forcing factors influence the dynamics of
110   compound flooding.

111   **2- Methods**

112   We apply an analytical approach to investigate the TWL caused by river discharge, tides, and surge
113   in an idealized estuary. Various forms of one-dimensional analytical solutions of tidal wave
114   propagation have long been used for idealized and real estuaries (e.g., Dronkers, 1964; Prandle
115   and Rahman, 1980; Jay, 1991; Friedrichs and Aubrey, 1994; Savenije, 1998; Lanzoni and
116   Seminara, 1998; Godin, 1999). More complex idealized tidal models investigate overtide
117   generation and evolution (e.g., Chernetsky et al., 2010), the effects of variable cross-section and
118   bottom slope (e.g., Savenije et al., 2008, Kästner et al., 2019), and the effects of multiple tidal
119   constituents and river discharge (Giese and Jay, 1989; Buschmann et al., 2009). Other studies have
120   used a tidal model combined with regression analysis (e.g., Godin, 1999; Kukulka and Jay, 2003a)
121   to investigate river discharge effects. Such idealized models, by the parameter space analyzed, can
122   be used to obtain fundamental insights into how long-waves in estuaries are affected by depth,
123   convergence, friction, and boundary forcing.

124   In our approach, we develop an analytical model which is driven by three sinusoidal constituents
125   and a constant river discharge. Our approach idealizes storm surge as the sum of two sinusoids,
126   and neglects factors, such as the potential role of wetlands as a storage reservoir, in order to gain
127   insight into some of the important, along-channel factors that govern the system response to a
128   compound event. Similarly, we neglect processes such as Coriolis acceleration and gravity waves,

129   and focus on the specific case of an incident, non-reflected long-wave that propagates from the
130   coast in the landward direction and is eventually completely damped out. Moreover, we simplify
131   our approach by considering only constant river flow conditions, a valid approximation for
132   situations in which the time scale of a river flood event is much longer than a storm surge.

2-1-   Analytical model

134   We use an idealized one-dimensional analytical model developed by Familkhalili et al., (2020) to
135   investigate how combinations of tides, storm surge, and river flow affect water levels in an estuary.
136   In this model, storm surge is approximated as the sum of a primary and a secondary sinusoidal
137   wave. A third sinusoidal frequency is reserved for the M_2 tidal constituent. Hence, the resulting
138   model is conceptually similar to the multi-tide constituent model developed by Giese and Jay
139   (1989) and the three-wave model of Buschman et al., (2009), with the distinction that two of the
140   waves are based on the amplitude and timescales of meteorologically induced storm surge rather
141   than an astronomical tide with a known frequency.

142   One-dimensional long wave propagation along an idealized, funnel-shaped estuary is described by
143   the cross-sectionally integrated equations of mass and momentum conservation (e.g., Jay, 1991;
144   Kukulka and Jay, 2003a; Familkhalili et al., 2020):

145
$$\frac{\partial Q}{\partial t} + \frac{\partial}{\partial x}\left(\frac{Q^2}{A}\right) + gA\frac{\partial \xi}{\partial x} + bT = 0 \tag{1}$$

146
$$\frac{\partial Q}{\partial x} + b\frac{\partial \xi}{\partial t} = 0 \tag{2}$$

147   where Q is cross-sectionally integrated flow and is the summation of the river and tidal transports
148   $(Q_R + Q_T)$, t is time, x is the longitudinal coordinate measured in landward direction (see Fig.
149   1a), b is width, g is the acceleration due to gravity, A is channel cross-section, ξ is tidal water level
150   elevation, T is the bed stress divided by water density $(\frac{\tau}{\rho} = C_d|u|u)$, C_d is a drag coefficient, and
151   $u = Q/A$ is the velocity. The absolute value of u is assigned to preserve the directionality of stress.
152   For simplicity, depth is assumed constant and channel width is allowed to vary exponentially with
153   respect to the longitudinal coordinate x (i.e., $b_{(x)} = B_c + (B_0 - B_c)e^{(-\frac{x}{L_e})}$, see Fig. 1a). Following
154   Familkhalili et al (2020), we set B_0=5 km and assume that the estuary section of the model domain
155   is 1.5 times the convergence length which determine a constant river width of ~1100 m. The
156   constant depth channel is routed upstream for 100 km, to enable the tide wave to dissipate and
157   prevent reflection off an upstream boundary. The tidal amplitude to depth ratio $(\frac{\xi}{h})$ is assumed
158   small, and river flow (Q_R) is held constant (e.g., Kukulka and Jay, 2003a; Familkhalili et al., 2020).
159   Applying these assumptions and combining Eq. (1) and (2) yields the following differential
160   equation:

161
$$\frac{\partial^2 Q_T}{\partial x^2} - \frac{1}{b}\frac{\partial b}{\partial x}\frac{\partial Q_T}{\partial x} - 2\frac{1}{gh}U_R\frac{\partial^2 Q_T}{\partial x\partial t} + 2\frac{1}{gh}U_R\frac{1}{A}\frac{\partial A}{\partial x}\frac{\partial Q_T}{\partial t} - \frac{1}{gh}\frac{\partial^2 Q_T}{\partial t^2} - \frac{b}{gh}\frac{\partial T}{\partial t} = 0 \qquad (3)$$

162 We linearize the frictional term ($T = C_d|u|u$) using Chebyshev polynomials (Dronkers, 1964) to
163 approximate the frictional term, $u|u|$. Following Godin (1991, 1999), only the first and third order
164 terms of the dimensionless velocity are retained, yielding:

165
$$\frac{u|u|}{U_{(x)}^2} \approx Au' + Bu'^3 \qquad (4)$$

166 where: $A = \frac{16}{15\pi}$, $B = \frac{32}{15\pi}$, $U_{(x)}$ is the maximum value of the total current ($U_R + U_T$) and is a
167 function of x, and u' is a non-dimensionalized velocity defined as $\frac{u}{|U_{(x)}|}$ (Doodson, 1956; Godin,
168 1991). See Familkhalili et al., (2020) for additional details.
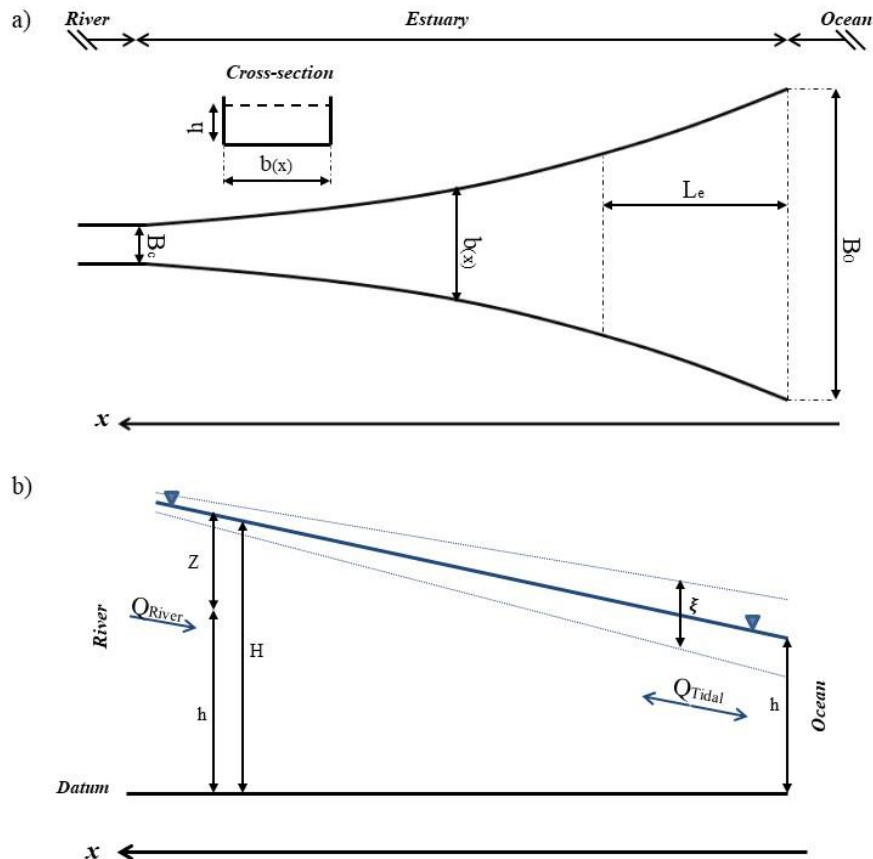
169

170   Figure 1; (a) Idealized bathymetry and plan view of the conceptual model and (b) definition of the water surface slope,
171   modified from Kukulka and Jay (2003b). Along channel direction x is upstream with $x =0$ at the ocean.

172   The sectionally and vertically averaged velocity term in Eq. (3) ($u = Q/A$) is decomposed into three
173   sinusoidal wave components and a constant river discharge:

$$u = u_r + \sum_{i=1}^{3} u_i cos(\omega_i t + \phi_i) \qquad (5)$$

174   where u_r is the river flow velocity, and u_i , ω_i, ϕ_i are velocity amplitudes, frequencies, and
175   phases, respectively. Although river discharge is not constant on the time scale of weather systems
176   (5-7 day) and seasonal time scales, we assume for simplicity that the change over a tidal cycle or
177   storm surge wave (generally <2 day time-scale) can be neglected. This limits our analysis to river
178   systems with a long-response time, i.e., it is inappropriate for short, steep, flashy systems with
179   flood time scales < 2 days.

180   We use a multi-segment approach (Dronkers, 1964), to divide the model domain into N segments,
181   each has a constant depth and exponentially varying width. This approach produces a system of
182    $2N$ linear equations with $2(N$-1) internal, one seaward, and one landward boundary conditions. The
183   landward of our analytical model is forced by a no-reflection condition with constant discharge
184   and the seaward boundary (see Fig. 1) is forced by 3 sinusoidal water level signals. One of the sine
185   waves represents the main semidiurnal tidal constituent, and two of the sine waves represent the
186   elevated water level of the surge signal in terms of primary and secondary components, denoted
187   by the *Pri* and *Sec* subscripts (Familkhalili et al., 2020):

$$Surge = \underbrace{A_{Pri}Cos(\omega_{Pri}t + \phi_{Pri})}_{Surge_{Pri}} + \underbrace{A_{Sec}Cos(\omega_{Sec}t + \phi_{Sec})}_{Surge_{Sec}} + \underbrace{C_1}_{Constant} \qquad (6)$$

188   where A is the amplitude, ω is the frequency, ϕ is the phase, and C_1 is an arbitrary offset. For
189   simplicity, the surge is treated as a free wave within the model domain, i.e., we neglect the effect
190   of wind stress and any locally generated component of surge.

191   An example fit using two sinusoidal waves to a hurricane surge is shown in Fig. 2. The surge signal
192   is calculated by subtracting predicted tide from observed water level at Lewes, DE (NOAA Station
193   ID: 8557380) and is caused by Hurricane Irene (August 2011). Fitting two sinusoidal waves
194   approximates the surge signal with correlation of R^2=0.95 and root-mean-square-error of 0.05 m
195   (Fig. 2). The fit is valid for the time period that the surge remains above the dashed line.

196
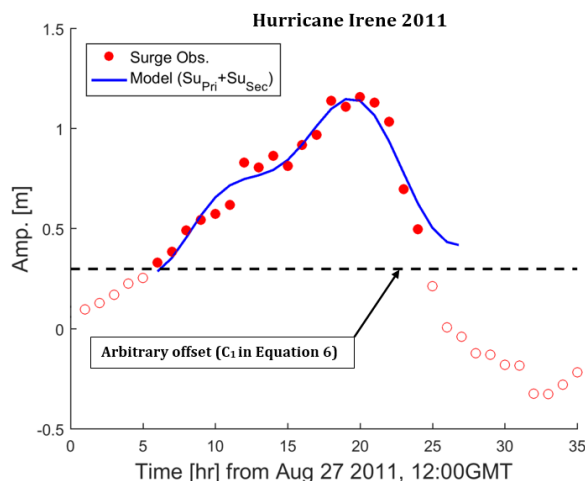
Figure 2; An example of decomposing surge into two sinusoidal waves. The red circles represent surge and are calculated by subtracting predicted tide from measured water level during Hurricane Irene (2011) at Lewes, DE (NOAA Station ID: 8557380). The blue line is the model fit that is the sum of Su_{Pri} and Su_{Sec} and black dashed line shows the threshold constant C_1, per Eq. (6).

Typical amplitudes, frequencies, and phases of the two component surge waves are determined by fitting two sinusoids to 354 storm surge events from Lewes, DE. These results are used to define the parameter space that we investigate (Sect. 2.4) and are typical of coastal storm surge characteristics on the mid-Atlantic Bight. Only significant events, with surges larger than 0.5 m, are fit. The largest resulting primary surge wave amplitude was about 1.1 m, larger than but of the same order as the main tidal constituent ($M_2 = 0.6$ m). The statistically significant fits ($R^2 = 0.91$) have average primary and secondary surge time scales of ~29 and ~16 h, respectively.

2-2-   River discharge effects on water surface slope

The presence of river discharge u_R and tidal velocities u_T causes stronger ebb currents ($u_R + u_T$) and weaker flood currents ($u_R - u_T$). The resulting non-linear interaction and increased friction typically reduces the tidal range, shifts the timing of high and low water (e.g., Godin, 1985; Hoitink and Jay, 2016), and generates tidal distortion (asymmetry) (Parker, 1991). The increased frictional effects also influence subtidal water levels, producing a larger river slope (Kulkulka and Jay, 2003b; Buschman et al., 2009; Talke et al., 2021). However, typical coastal plain systems in the western Atlantic have low river flow relative to tidal discharge amplitudes. For example, the ~200 m^3/s average annual discharge of the Saint Johns River Estuary, Florida, is about 5 % of total discharge (river + tides) (Talke et al., 2021). Similarly, the Delaware River Estuary has mean and median river flows at Trenton, NJ of ~340 m^3 s^{-1} and 285 m^3 s^{-1}, respectively, small compared to tidal flow of ~23×10^4 m^3 s^{-1} at the mouth (USGS, 2018; Munchow et al., 1992). The Cape Fear

220   River has an average river discharge of 268 m^3 s^{-1} (Familkhalili and Talke, 2016), which is less
221   than 5 % of total averaged ebb-tidal flow (Olsen, 2012).

222   River flow alters the water surface slope, and this behavior influences the spatial distribution of
223   total water level (e.g., Fig. 1b). Here, we use the tidally averaged one-dimensional equation of
224   motion to investigate water level gradients, following Kukulka and Jay (2003b) and Godin (1999).
225   For simplicity, no component of mean water level caused by the tidal Stokes drift is considered.
226   The parameter h is the mean depth of water, ξ is the tidal amplitude (small compared to depth), Z
227   is the perturbation in the water surface elevation due to river discharge Q, and is assumed to be
228   much smaller than h. In this study, river flow velocity (applied at the upstream boundary) is
229   parameterized as the ratio of the river velocity magnitude to the magnitude of the major tidal
230   component velocity at the ocean boundary (i.e., $\frac{|u_r|}{|u_{D_2}|}$ or θ hereafter). To evaluate the effect of
231   elevated river discharge, we consider a river flow ratio of 0 to 1. The ratio of $\theta=1$ represents a case
232   in which river and tidal flows are comparable, and thus is outside the zone of our assumptions;
233   however, comparisons with numerical model results suggest that results below this ratio are
234   reasonable (see Sect. 2.3). Therefore, we assess both low-flow conditions and conditions in which
235   the river flow is comparable to tidal discharge.

236   Previous studies (e.g., Ralston et al., 2019; Helaire et al., 2019; Talke et al., 2021) showed that
237   reduced friction due to increased channel depth can alter the tidally averaged water level gradient
238   ($\frac{\partial Z}{\partial x}$, Fig. 1b). River slope can be determined from the one-dimensional equation of motion (Godin,
239   1999):

$$\underbrace{\frac{1}{g}\frac{\partial \bar{u}}{\partial t}}_{\substack{Local \\ acceleration}} + \underbrace{\frac{\bar{u}}{g}\frac{\partial \bar{u}}{\partial x}}_{\substack{Convective \\ acceleration}} = -\underbrace{\frac{\partial H}{\partial x}}_{\substack{Pressure \\ gradient}} - \underbrace{\frac{\bar{u}|\bar{u}|}{C_h^2(h+\xi)}}_{Friction} \qquad (7)$$

240   where $\bar{u}$ is tidally averaged value of the current at x, g is the acceleration due to gravity, C_h is
241   Chézy coefficient, and h is the mean depth of water. Scaling the terms in Eq. (7) using values
242   typically found in estuaries (e.g., Godin and Martinez, 1994; Kukulka and Jay, 2003b, Buschman
243   et al., 2009) shows that zero-order balance is between the pressure gradient and the friction term,
244   so that the entire left-hand side of Eq. (7) can be neglected as small, though the convective term
245   may be locally important in real systems with complex geometry (e.g., Helaire et al., 2019).

246   Since the cross-sectional area in our model varies smoothly (exponentially) over a large length
247   scale, our approach neglects convective effects. We neglect the riverbed slope, since the bed slope
248   in estuaries is typically small (order 10^{-5}), particularly in modern dredged systems (see e.g., Talke
249   et al., 2021). Within the upstream reaches of tidal rivers, the bed slope often increases and is
250   important dynamically (Kästner et al., 2019); therefore, we restrict our analysis and interpretation

251   to estuarine reaches. As before, we assume that the tidal amplitude to depth ratio ($\frac{\xi}{h}$) is small. Given
252   these assumptions, we simplify Eq. (7) to the following balance (Godin and Martinez, 1994):

$$\frac{\partial \overline{H}}{\partial x} = -\frac{\overline{u}|\overline{u}|}{C_h^2 \overline{h}} \tag{8}$$

253   where $\overline{H}$ is elevation and $\overline{h}$ is the mean water level (the overbar denotes the tidally averaged value).
254   The low-frequency momentum Eq. (8) shows that the surface slope is defined by the bed stress
255   term. Considering the first and third terms in Eq. (4), we use a quasi-linear form of the quadradic
256   velocity term (i.e., $\overline{u}|\overline{u}|$) to solve the equation (see Sect. 2.1).

257   **2-3-   Model validation**

258   The tide-surge analytical model was previously compared against the tidal amplitude variation of
259   two one-constituent analytical models (the Toffolon and Savenije, 2011 and Jay, 1991 tidal
260   solutions) and idealized Delft-3D numerical model results (see Familkhalili et al., 2020). Results
261   showed that our analytical model is capable of capturing wave amplitudes that are in good
262   agreement with numerical models results. Here we update the validation to include the effects of
263   river flow and compare our results against idealized Delft-3D numerical model results that are run
264   under the same bathymetry and forcing. Analytical/numerical comparisons were made for a
265   weakly convergent and strongly dissipative estuary with constant depth of 5m and a width profile
266   defined by B_0 = 5 km, L_e = 80 km, and B_c= 400 m (see Fig. 1). Both analytical and numerical
267   models are forced by the K_1, M_2, and M_3 tidal constituents with amplitudes of 0.25, 0.5, and 0.25
268   m, respectively at the ocean boundary, two of which (K_1 and M_3) combined represent a surge
269   wave. We further analyze the numerical model results by using harmonic analysis (e.g., Leffler
270   and Jay, 2009).

271   Figure 3 shows the spatial pattern of the dominant tidal constituent (M_2) amplitude normalized by
272   its value at the estuary mouth. The analytical model results closely resemble the numerical model
273   results with a root-mean-square error of 0.02 m for both the three-wave model with and without
274   river flow (blue and red colors in Fig. 3), showing that this idealized analytical model can properly
275   estimate spatial variability of surge along an estuary.

276
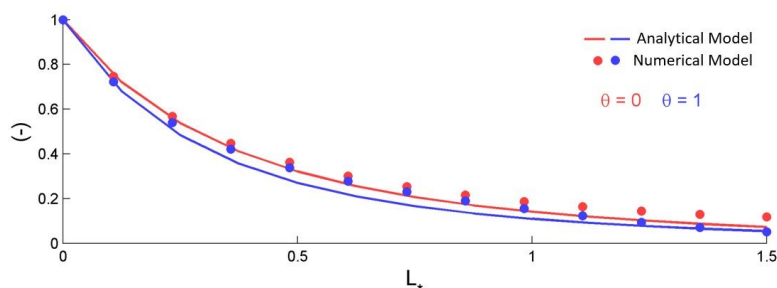
Figure 3; Dominant tidal constituent (M_2) amplitude in a 5 m deep estuary for three tides models (K_1, M_2, and M_3) with and without river flow (θ=0-1). The x axis is the estuary length normalized by the convergence length scale ($L_* = x/L_e$) and the vertical axis is normalized by M_2 amplitude at the ocean boundary (L_*=0).

In addition, results for tidally averaged water levels (i.e., Z; see Fig. 1) under conditions of tidal and river-flow forcing are consistent with numerical models. The water level profiles vary with θ (flow) for both the analytical model (dashed lines) and the numerical model (solid lines) as shown in Fig. 4 for a weakly convergent estuary. In general, the analytical model slightly underestimates numerical results. The RMSE between the numerical and analytical surface profiles are 0.03, 0.08, 0.09, 0.10m for a θ of 0, 0.25, 0.5, and 1.0, respectively, or roughly 3-8 % of the total super-elevation above sea-level (Fig. 4a).
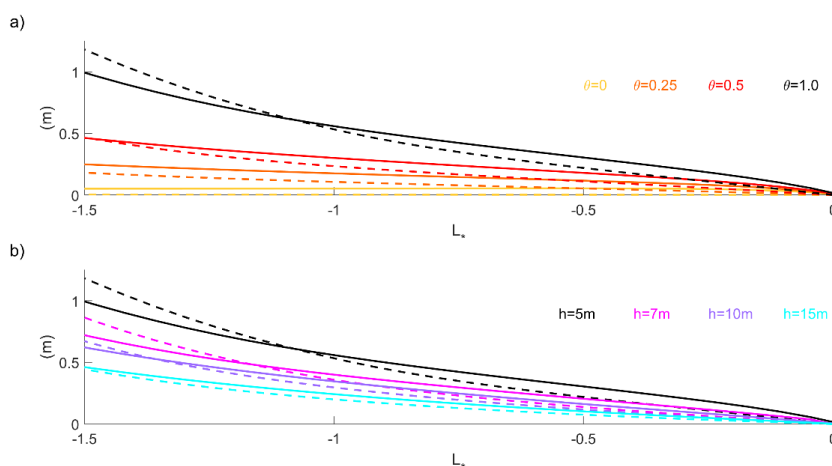
Figure 4: (a) The importance of river flow (i.e., θ at L_*=1.5) for 5m depth and (b) the importance of channel depth for θ=1 in an idealized three sinusoidal waves model. Vertical axis is tidally averaged water level and horizontal axis represents dimensionless coordinate system of $L_* = x/L_e$. Solid and dashed lines represent numerical and analytical model results, respectively. The black solid and dashed lines represent same scenario (h=5 m, θ=1) in both (a) and (b).

Larger river discharge (greater θ) produces higher mean water levels (Z), as expected (see Fig. 4a). As river discharge increases (Fig. 4a), the depth averaged velocity increases, and a larger water surface slope ($\frac{\partial \bar{H}}{\partial x}$) is needed to balance the Eq. (8). Equation (8) also shows that a shallower estuary (smaller h) has a similar impact on water surface slope as increasing averaged river flow velocity (larger u) (see also Talke et al., 2021). Shallower depth (h) causes a steeper surface slope (Eq. (8)), because a larger pressure gradient is required to drive the flow downstream (see also Hoitink and Jay, 2016). Similarly, increased depth reduces frictional effects and result in lower mean water levels (Fig. 4b). For example, increasing depth from h=5 m (black dash line in Fig. 4b) to h=10 m results in an up to 0.55m reduction in mean water level (at L_* =1.5). The effects of deeper shipping

302 channel on mean water levels are also observed and modeled in the Hudson and Columbia River
303 estuaries (Ralston et al., 2019; Helaire et al., 2019).

304 Each incremental increase in depth produces a smaller change in the slope (dZ/dL_*); for example,
305 the change in the water level profile between 5 m and 10 m is larger than a similar proportional
306 change from 10 m to 15 m (Fig. 4b). Consistent with other studies (e.g., Kukulka and Jay, 2003b;
307 Hoitink and Jay, 2016), both the analytically and numerically modeled water level slope (dZ/dL_*)
308 is largest upstream and becomes significantly less near the coast. This is driven by the decreased
309 river velocity (and friction) due to the increase in cross-sectional area in the estuary. Therefore,
310 we expect that varying the forcing conditions will most impact mean water levels more upstream,
311 due to greater total river velocity magnitudes in the landward part of the system.

312 **2-4-   Dimensional and non-dimensional parameter space studied**

313 We use our validated analytical model to further investigate the effects of channel depth, river
314 flow, channel width convergence, and surge time-scale on the spatial evolution of water levels
315 along estuaries. For all simulations, the primary tidal constituent period and amplitude are fixed to
316 12 h (i.e., a semidiurnal or D_2 wave) and 0.5 m, respectively, a value that is typical of the semi-
317 diurnal tide wave on the U.S. East Coast (Table 1). To study the effects of width convergence, we
318 test both weakly (L_e=80 km) and strongly convergent (L_e=20 km) conditions (see e.g., Jay, 1991;
319 Lanzoni and Seminara, 1998). Table 1 shows the parameter space used in the model. The primary
320 and secondary surge amplitudes are set to be 0.5 and 0.25 m, respectively (Eq. (6)) and the estuary
321 mouth (B_0) is assumed to have a width of 5 km. Sensitivity analysis is done by varying the
322 parameters in Table 1 individually, with other parameters held constant, resulting in a total of 128
323 parameter combinations (i.e., four different values for depths, four different values for river flow,
324 four different time scales combination, and two convergence length scales).

325   Table 1: Parameter space used in analytical model

Channel Depth (m)	5, 7, 10, 15
Su_{Pri} *Amp.* (m)	0.5
Su_{Sec} *Amp.* (m)	0.25
$\begin{pmatrix} Su_{Pri} \ Time\ Scale\ (h) \\ Su_{Sec}\ Time\ Scale\ (h) \end{pmatrix}$	$\begin{pmatrix}12\\6\end{pmatrix}, \begin{pmatrix}24\\12\end{pmatrix}, \begin{pmatrix}48\\24\end{pmatrix}, \begin{pmatrix}72\\36\end{pmatrix}$
D_2 *Amp.* (m)	0.5
D_2 *Time Scale* (h)	12

Upriver flow velocity ($\theta = \frac{|u_r|}{|u_{D_2}|}$) at L_*=1.5	0, 0.25, 0.5, 1
L_e Convergence length scale (km)	80 (weakly convergent), 20(strongly convergent)

326

327 Non-dimensional variables provide insights into which parameters produce the most effect on
328 system response. From the scaling of Eq. (3) (see also Familkhalili et al., 2020), we derive the
329 three most relevant independent non-dimensional variables:

- 330 • Parameter (Ω) represents the ratio of Su_{Pri} time scale to D_2 period and represents the
  331 influence of primary surge wave time scale on tide-surge interactions.
- 332 • The friction number ($\psi = \frac{C_d \xi \omega^2 L_e^3}{gh^3}$) shows the effects of changing surge wave
  333 properties, which are influenced by depth (h), surge frequency ($\omega = \frac{1}{T}$), and
  334 convergence length-scale (L_e); all affect the damping or amplification of surge
  335 waves.
- 336 • Parameter (θ) represents the ratio of upriver velocity (at L_*=1.5) to the major tidal
  337 component (D_2) velocity at the estuary mouth.

338 For plotting purposes, we define two additional non-dimensional numbers: Su_{Pri} normalized
339 amplitude ($A_* = \frac{Amp. Su_{Pri}}{Surge\ Amp.\ at\ Boundary}$) and a dimensionless coordinate system of $L_* = x/L_e$,
340 where L_* is normalized length.

341 In our models we assume that the two surge waves are symmetric with a phase lag (ϕ in Eq. (5))
342 of zero degrees between Su_{Pri} and Su_{Sec}, resulting in a repeating and symmetric storm surge wave
343 (see Fig. 5). This simulates a storm surge in which there is initially a draw-down in water level,
344 followed by the positive storm surge. To test the most frictional case, we also define the relative
345 phase lag between the D_2 wave and surge to be zero.
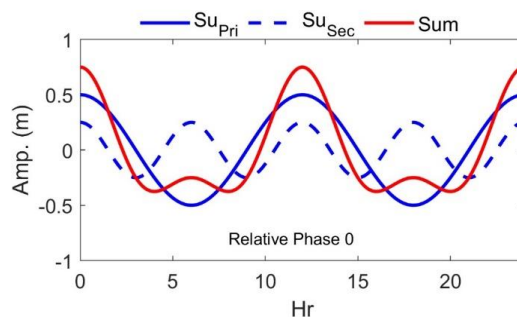
346

347   Figure 5; A symmetric surge wave which is the result of two sinusoidal waves (i.e., $Surge = Su_{Pri} + Su_{Sec}$).

3- Results and discussion

349   We employ the validated model to study how bathymetry, river discharge, and surge characteristics
350   affect water floods in an idealized estuary. First, the effects of surge amplitude and time scale on
351   water levels are examined. Then, the effects of river discharge and width convergence on surge
352   amplitude are presented, and finally compound flooding of tide, surge, and river flow is
353   investigated.

3-1- Effects of wave characteristics on water level

355   The influence of wave characteristics (i.e., time scale and magnitude) on tidally averaged water
356   level is tested by modeling a set of waves with time scales of 12 h and 24 h and amplitudes of 0.5
357   m and 1 m at the ocean boundary. Model results confirm, as suggested by the friction number (ψ),
358   that increasing wave time scale ($T = \frac{1}{\omega}$) or decreasing wave amplitude (ζ) has similar effect as
359   increasing depth (h) and therefore would result in lower mean water levels (see Fig. 6). Figure 6
360   shows that increasing wave time scale from 12h (red lines) to 24h (blue lines) would reduce the
361   mean water level at L_* =1.5 from 0.75 m to 0.5 m, and from 1.56 m to 1.10 m for wave amplitudes
362   of 0.5 m and 1 m at the ocean boundary ($L_* = 0$), respectively. In other words, for the same
363   boundary amplitude, a shorter time scale wave produces larger mean water levels landward.
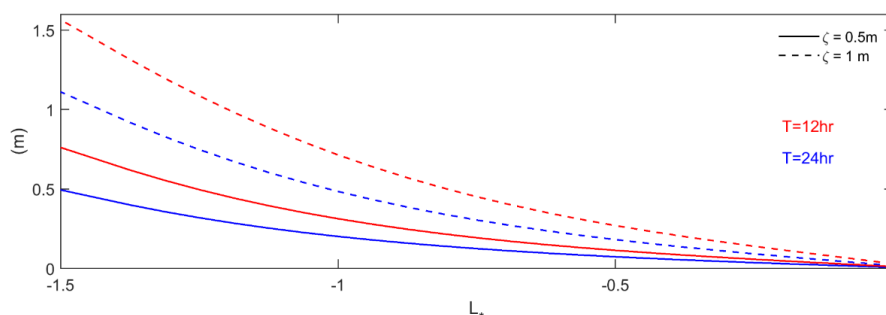
364

365   Figure 6: The effects of wave time scale (i.e., 12 h and 24 h) and amplitude (0.5 m and 1m at the ocean boundary $L_* =$
366   0) on tidally averaged water level for 5 m depth channel in an idealized one sinusoidal wave model for θ=1. Vertical
367   axis is tidally averaged water level, and the horizontal axis represents the estuary length normalized by the
368   convergence length scale (i.e., $L_* = x/L_e$).

3-2- Frictional effects of river discharge on surge amplitude

370   The rate at which a surge decays away from the ocean entrance varies with river flow and surge
371   time scale. Figure 7 shows the effects of river discharge and surge time scale on the *e*-folding

length-scale of Su_{Pri} normalized amplitude ($A_* = \frac{Amp.}{Amp.\ at\ ocean\ boundary}$) (*e*-folding is defined as the lengthscale required to get to $1/e\sim 38\ \%$ of boundary values). The longer the wave period, the more slowly surge amplitude A_* decreases as the surge moves landward (keeping all other variables constant). For example, Fig. 7a shows that a 12h ($\Omega = 1$) surge amplitude reaches an *e*-folding reduction in amplitude at ~$0.4L_*$ compared to ~$0.9L_*$ for the 72 h ($\Omega = 6$) surge. The lower rate of spatial decay of surge amplitude for lower frequency surge waves is caused by their lower velocity and consequent smaller frictional effects.

Model results also show that higher river discharge will increase the damping of surge amplitudes (Fig. 7). When ($\theta = 0$), river flow is zero and only tide-surge nonlinear interactions can occur. Hence, surge amplitudes decay more slowly for $\theta = 0$ than for $\theta > 0$ (compare the $\theta = 0$ and $\theta = 1$ cases in Fig. 7). The slanted contour lines highlight the effects of river flow; as θ increases, the *e*-folding length-scale of normalized amplitude (A_*) reduces for all surge time scales ($\Omega = 1-6$) (Fig. 7a-d). Adding river flow to a surge with a primary time-scale of 12 h ($\Omega = 1$) reduces the *e*-folding scale of damping from $0.4L_*$ ($\theta = 0$) to $0.34L_*$ ($\theta = 1$), for the 5 m depth case (~15 % decrease; Fig. 7a). The percent decrease in the *e*-folding scale is larger in a deeper, 15m channel, and decreases from $1.15L_*$ to $0.95L_*$ (~18 % decrease; Fig. 7d).

Surge amplitudes also decay more slowly (larger *e*-folding) in a deeper channel for all surge time scales (Fig. 7). Sensitivity studies show that the largest difference in normalized amplitude between a 12 h ($\Omega = 1$) and 72 h ($\Omega = 6$) surge occurs at larger depth ($h=15$ m) with changes of ~$1L_*$ to $3.5L_*$ in the *e*-folding length-scale of damping (Fig. 7d). Increasing the river discharge relative to the M_2 velocity (larger θ) reduces the amplification of the surge wave and therefore the *e*-folding length scale of A_* reduces from ~$3.5L_*$ to ~$2.4L_*$ for Su_{Pri} of 72 h (Fig. 7d).
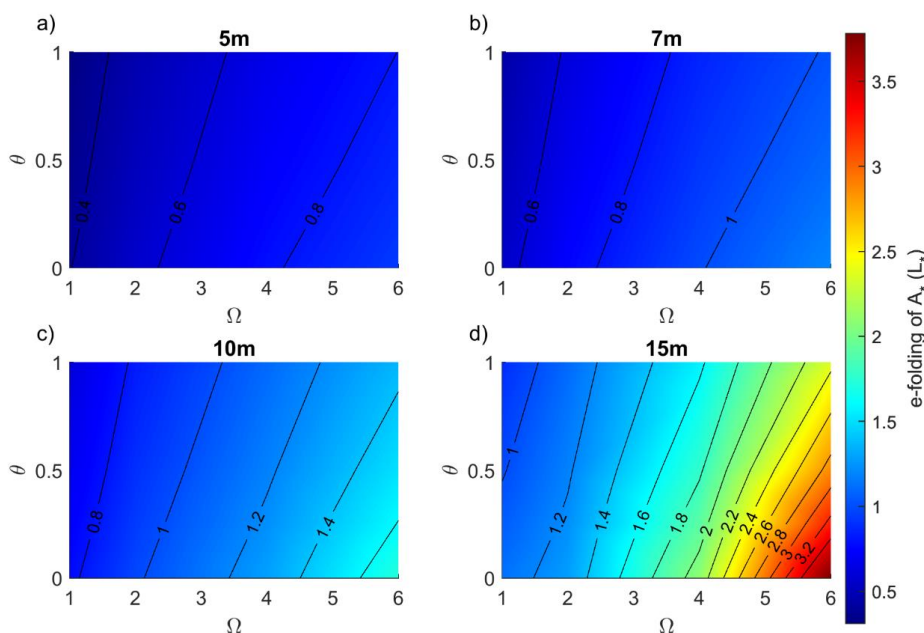
Figure 7: The effects of river flow ($\theta = \frac{|u_r|}{|u_{D_2}|}$) and surge periods ($\Omega = \frac{Period\ Su_{Pri}}{Period\ D_2}$) along an idealized weakly convergent estuary for channel depth of (a) 5 m, (b) 7 m, (c) 10 m, and (d) 15 m. The color scaling represents the e-folding length-scale of primary surge normalized amplitude (A_*).

3-3- Effects of width convergence on surge amplitude

Long-wave propagation along an estuary is characterized by a balance of inertial effects, friction, and convergence. Figure 8 shows the normalized amplitude (A_*) of the primary surge wave for weakly convergent (left panel, 8a and 8c) and strongly convergent estuaries (right panel, 8b and 8d), for a 12h surge time scale (Ω =1). The contours represent the e-folding length scale of primary surge normalized amplitude and the x-axis represents the dimensionless coordinate system of $L_* = x/L_e$. The factor 4X change in convergence length scale from 80km (Fig. 8a, 8c) to 20 km (Fig. 8b, 8d) alters the friction scale (ψ) by a factor of 64.

The convergence of an estuary influences surge amplitudes (Fig. 8), similar to its well-known effects on tidal amplitudes (e.g., Jay, 1991). All surge amplitudes decrease landward for all depth cases in a weakly convergent (L_e=80 km) estuary; effectively, convergence effects are much smaller than the bed friction and gravity effects and therefore long-wave amplitudes decrease (Fig. 8a and 8c). Under strongly convergent conditions with no river flow, the primary surge amplitude decays less quickly in a deeper channel as it moves upstream than under weakly convergent condition (see Fig. 8a, b), and can even increase in the inland direction (see Fig. 8b). By contrast, increased river discharge produces greater damping in the surge wave (compare Fig. 8a and 8c, or

414   Fig. 8b and 8d). For example, for friction factor of ψ =0.5 (h = 6.5 m) and a location of L_* = 1,
415   the surge wave has damped to 60 % of its boundary value when the tidal to river flow ratio is θ=1
416   (Fig. 8d) but is at 70 % of its boundary value when there is no river discharge (Fig. 8b). Hence,
417   increasing river flow and decreasing channel depth both cause larger damping in the surge wave.
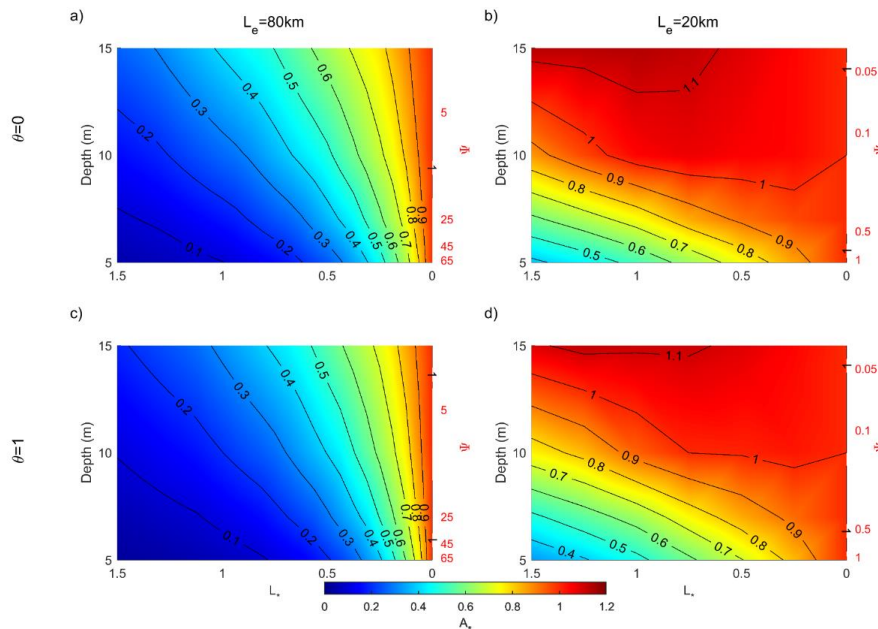
418

419   Figure 8: The effects of convergence length scale and river discharge on primary surge (12h, Ω =1) amplitude (A_* is
420   normalized amplitude) along a weakly convergent estuary, L_e=80 km (subplots a, c) and strongly convergent estuary,
421   L_e=20km (subplots b, d). Left hand side vertical axis is channel depth and right-hand side vertical axis is the
422   corresponding non-dimensional friction number ($\psi = \frac{C_d \xi \omega^2 L_e^3}{g h^3}$) and horizontal axis represents dimensionless
423   coordinate system of $L_* = x/L_e$.

424   **3-4-   Combined effects of tide, surge, and river flow on total water levels**

425   We next investigate how variations in river flow influence the Total Water Level (TWL), which is
426   the summation of tide, storm surge, and river discharge effects (TWL=T+SS+R). The highest
427   possible total water level (HTWL) during such a compound event occurs when the tide (D_2) and
428   surge have zero relative phase (i.e., the surge occurs at high water) and when the peak river flow
429   occurs at the same time. Because the timing of a meteorological event is usually random relative
430   to tides, and because peak surge usually precedes peak river discharge, HTWL rarely if ever
431   occurs. However, it is a useful metric of the potential flooding. Such a worst-case scenario could
432   occur, for example, when multiple storms occur in close succession. The HTWL therefore provides
433   a way to compare different parameter regimes and evaluate the effect of long-term changes in the
434   geometry of an individual estuary.
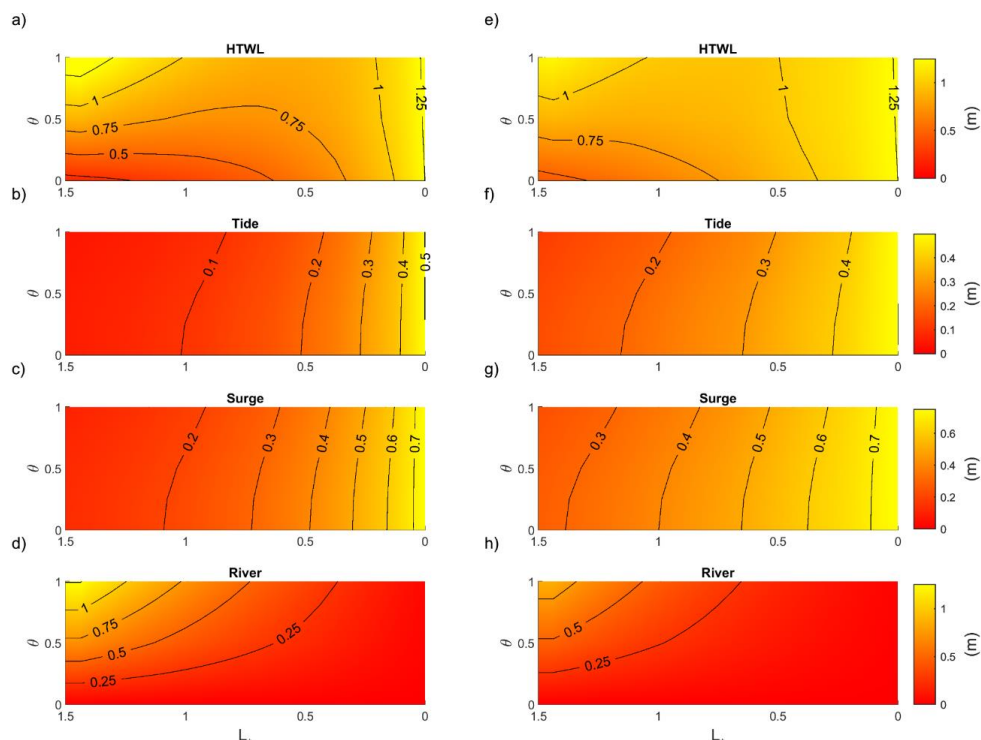
435
436 Figure 9: Combined contribution of tide, surge, and river flow to water level for depths of 5 m (left panel subplots)
437 and 10 m (right panel subplots). Colors and the labeled contours denote water level. The total water level (a and e) is
438 the combination of tidal amplitude (b and f), surge amplitude (c and g) and water level from river discharge (d and
439 h). The period of the primary surge (Su_{Pri}) is 24 h, the convergence length scale is 80km, the x-axis represents
440 dimensionless coordinate system of $L_* = x/L_e$ (origin at estuary mouth, on right-hand side) and the y-axis shows the
441 non-dimensional river flow ($\theta = \frac{|u_r|}{|u_{D_2}|}$). Note the difference in color-bar scales between plots.

442 The HTWL (Fig. 9a and 9e) follows a pattern set by the contradictory effects of river flow and
443 marine forcing (tides and surge). Far upstream ($L_* = 1.5$), river water levels are the largest factor,
444 particularly for larger θ, and decay in the downstream direction (Fig. 9d and 9h). The surge and
445 tidal components of water level (e.g., Fig. 9b, 9c) decay in the opposite direction, from the oceanic
446 boundary towards the upstream boundary. For larger river flows (~θ>0.5) and this parameter
447 space, the counteracting factors produce a minimum HTWL in the middle part of the domain (L_*=
448 0.5-1.0). For small river flows, water levels monotonically decrease in the upstream direction.

449 Importantly, the HTWL is not merely the superposition of river flow, tide, and surge effects,
450 considered in isolation. Rather, as shown by the non-vertical contour lines for tides and surge (e.g.,
451 Fig. 9f and 9g), increases in the relative influence of river flow (larger θ) tend to reduce the
452 magnitude of tides and surge (see also Helaire et al., 2020). By contrast, increases in long-wave

453   magnitudes (tides, surge) at the ocean boundary increase the tidally averaged water level profile,
454   as already established (Fig. 6; see also Buschman et al., 2009 and Talke et al., 2021).
455   Simultaneously, long-wave magnitudes decrease more quickly, the larger they are at the estuary
456   boundary (see also Familkhalili et al., 2020). Effectively, each component of water level influences
457   the other, and itself: for example, tides within the domain depend on self-interaction (e.g., the
458   boundary magnitude matters), and also on tide-surge and tide-river interaction. While the overall
459   influence in terms of magnitude is relatively minor for the parameter space in Fig. 9, these
460   observations show that non-linear tide-surge-river interactions during a compound event cannot
461   be neglected.

462   Changes in the depth of an estuary, whether by dredging, sea-level rise, or morphodynamic change,
463   also exert a strong, spatially variable influence on the HTWL (Fig. 9 and 10). When depth is small
464   (5m; Fig. 9a), the HTWL is greater in the upstream domain ($L_* = 1.5$ and $\theta > 0.5$) than in a larger
465   depth case (10m; Fig. 9e). This occurs because a larger average river slope is needed to push the
466   same amount of water seaward when depth is small, as suggested by Eq. (8) (see also Talke et al.,
467   2021). However, smaller depths also lead to greater dissipation and frictional effects in the tide
468   and surge wave, due to the same reduction in hydraulic drag (compare right-hand and left-hand
469   side of Fig. 9, and their difference (Fig. 10)). Hence, tide and surge amplitudes increase when
470   depth is increased, for all river discharges ($\theta = 0-1$; Fig. 10b, c). The percent increase is less for
471   higher river discharge; this is shown by the contours that slant rightwards (Fig. 10b and 10c).
472   Further, both tides and surge show a region of maximum change, located in mid-estuary (between
473   L_* 0.5 to 1; Fig. 10). Near the ocean boundary, changes are relatively small, also in percentage
474   terms. Far upstream, the percent change in tidal range may still be significant, but the magnitudes
475   themselves are small (see also Talke et al., 2021).

476   The differences in the response of river flow and storm surge to a depth increase lead to a *crossover*
477   *point,* which we define as the location in which river flow effects are larger than marine effects,
478   for a given set of forcing conditions (see the zero-contour line in Fig. 10a). Since the crossover
479   point moves upstream as depth increases (Fig. 11), processes such as dredging, erosion, or sea-
480   level rise that increase depth can alter the relative influence of marine and river effects, for a given
481   storm surge and river flow. Similarly, a decrease in mean river discharge, as has occurred in many
482   places due to flow regulation, may also cause a landward migration in the crossover point (Fig.
483   11).

484   Other factors that influence long-wave amplitudes also influence the crossover point, including the
485   time scale of the surge (Fig. 7), convergence L_e (Fig. 8), the boundary amplitude, and the relative
486   phasing of tides and surge (see Familkhalili et al., 2020). The influence of many of these factors
487   is explained by considering the non-dimensional friction number ($\psi = \frac{c_d \xi \omega^2 L_e^3}{gh^3}$) (see Sect. 2.1). This
488   number suggests that increases in channel depth (h), wave time scale ($T = \frac{1}{\omega}$), and decreased length
489   scale (L_e) have similar effects on wave amplitudes. For example, increasing the depth from 5 m

490 (ψ = 69) to 15 m (ψ = 2.6) causes A_* (i.e., normalized amplitude by ocean boundary amplitude)
491 to increase from ~0.06 to 0.26 (Fig. 8a). Similarly, changing the surge time scale from 12 to 60 h
492 (ψ = 69 to 2.8) changes A_* from ~0.06 to 0.22 for a 5 m channel depth.

493 Others such as Bilskie and Hagen (2018) have defined flood zone transitions between marine and
494 fluvial dominance; close to coast, tide and surge based flooding dominates, while river floods
495 dominate far upstream. In between, there is a transition zone with compound flooding in which
496 both coastal and fluvial processes are important. Here, our model also suggests that the transition
497 zone may be sensitive to changes in estuary geometry, such as depth, in addition to being
498 dependent on the relative strength of river flow, tide, and surge amplitudes.
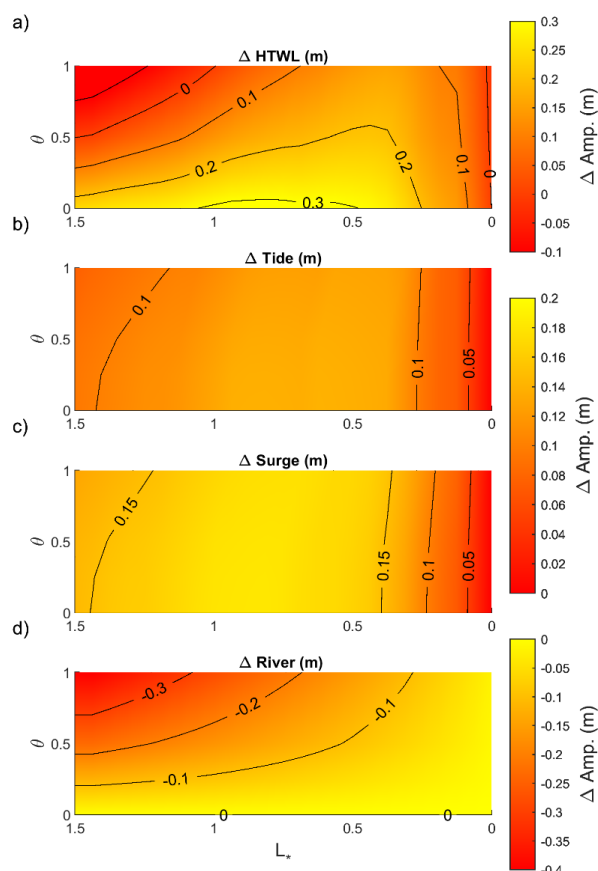
499

500 Figure 10: Comparison of contribution of tide, surge, and river flow to compound flooding between 5 m and 10 m
501 depth channel and Su_{Pri} = 24 h. Δ represents the amplitude difference of each subject (HTWL, tide, surge, and river

502   flow) between two controlling depths. The convergence length scale is 80km and x-axis represents dimensionless

503   coordinate system of $L_* = x/L_e$ and y-axis shows non-dimensional river flow ($\theta = \frac{|u_r|}{|u_{D_2}|}$).
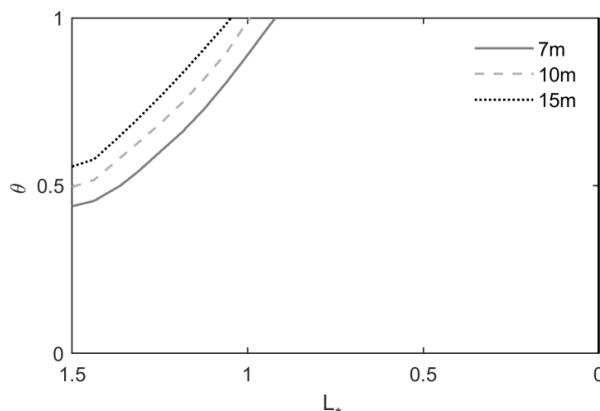
504

505   Figure 11: Crossover point location for 7-15m channel depth compared to 5m case, ($Su_{Pri} = 24$ h and $L_e = 80$ km). x-
506   axis represents dimensionless coordinate system of $L_* = x/L_e$ and y-axis shows non-dimensional river flow ($\theta =$
507    $\frac{|u_r|}{|u_{D_2}|}$).

508   **3-5-   Comparison with numerical model**

509   Our model provides insights into how and why changes to depth, surge time scale, and
510   convergence length-scale affect the damping/amplification of surge in real estuaries. For validation
511   and further insights, we compare the analytical results to the idealized numerical modeling of
512   Familkhalili and Talke (2016). As shown in Familkhalili and Talke (2016), the Cape Fear River
513   Estuary is an example of a strongly convergent estuary with an e-folding length scale of ~20km
514   upstream of river kilometer (Rkm) 12. Over the past 125 years, the shipping channel was increased
515   from 7m to 15m depth, which resulted in a near doubling of tidal range and a large (modeled)
516   increase in storm surge.

517   We next compare our analytical results at ~$L_* = 1.5$ with the results of Familkhalili and Talke
518   (2016) at Wilmington, NC, using a time scale of 12 h. For a shallow estuary of 7 m that is consistent
519   with late 19th century conditions in the Cape Fear, our results show that the storm surge wave is
520   damped by ~40 % (from 0.5 m to 0.3 m) between the coast and $L_* = 1.5$ (Fig. 8b, Fig. 12). This
521   damping is within the range of modeled results for a tropical storm surge at Wilmington ($L_* \sim 1.5$,
522   Fig. 12). In a modern configuration (mean depth = 15 m), the analytical model (this paper) finds a
523   12 % increase (i.e., $A_* = 1.12$) in surge amplitude, while the numerical model of Familkhalili and
524   Talke (2016) shows a range of $A_* = 0.55$-1.35 at Wilmington (Fig. 12). Hence, both the sense of
525   change and the order of magnitude of change is consistent between the numerical and analytical
526   model, improving our confidence in results. We conclude that in a shallow estuary the effects of
527   friction are dominant over the convergence and cause the wave amplitudes (tides and surge) to

528 decrease, while deepening the estuary may cause amplification of long-waves upriver of an
529 estuary. As shown in Fig. 8, the amplification in storm surge is particularly acute when the estuary
530 is highly convergent; hence, estuaries such as the Cape Fear may be particular to depth-induced
531 shifts in storm surge amplitudes.
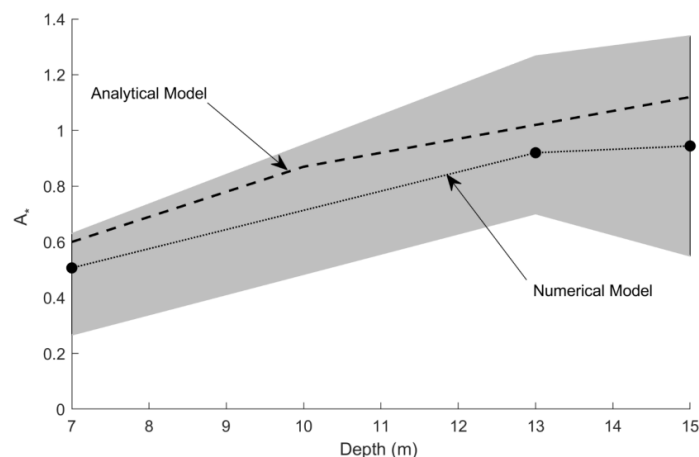
532

533 Figure 12: Numerical modeled storm surge at Wilmington, NC produced by tropical storm hurricane with mean
534 surge amplitude of 0.6m at ocean boundary (numerical model data from Familkhalili and Talke 2016). The fill area
535 around the mean is the range of results due to different relative phase of the storm surge and tide wave. The black
536 dashed line (labeled 'Analytical model') represents damping of a 12h surge with an amplitude of 0.5m (A_* is
537 normalized amplitude and equals one at the ocean boundary). The analytical model results are replotted from Fig.
538 8b.

4- Conclusion

540 In this study, we have applied a new river-tide-surge analytical model to investigate the
541 interactions of tide, surge, and river flow along idealized estuaries. We show that the rate of
542 damping in a storm tide (surge + tide) is sensitive to fluctuations of river discharge (Fig. 7),
543 alterations in the surge time scale (Fig. 7), and channel geometry changes (depth and width
544 convergence) (Fig. 8). Model results show that the crossover point, which is the location at which
545 the river flow effects are larger than marine effects, moves upstream as channel depth increases or
546 as river flow decreases (Fig. 11). Thus, the spatial variability in compound flood risk contributors
547 (i.e., tide, surge, and river flow) change when an estuary is modified, or river discharge changes.
548 Generally, increasing the surge time scale has a similar effect as increasing the depth; however,
549 we note that our model is slightly more sensitive to depth, due to the cubic relationship in the
550 friction term, rather than the squared effect of time scale. The non-dimensional friction number
551 (ψ) suggest that the effects of surge amplitude at boundary (ξ) and drag coefficient (C_d) have a
552 lesser, but still important, influence on the spatial damping of surge as the depth.

553 Globally, natural and local anthropogenic changes in estuaries (e.g., sea-level rise, channel
554 deepening for navigation and landfilling) produce alterations in tidal and surge amplitudes (see
555 review by Talke and Jay, 2020, and references therein). This study shows that river flow and its
556 interaction with tides and surge must also be considered when evaluating changes to water levels.
557 For example, increasing the river discharge relative to tide velocity reduces the amplification of
558 the surge wave. Moreover, channel deepening produces a reduction in the water level caused by
559 river discharge, leading to a domain in which channel deepening produces lower water levels
560 upstream but larger water levels in the estuary (Fig. 9-11; see also Helaire et al, 2019 and Ralston
561 et al., 2019). Our findings are consistent with other studies that find that reduced frictional effects
562 (e.g., caused by channel deepening) can cause increases to tides and surge (see e.g., Ralston et al.,
563 2019; Talke et al., 2021). Hence, the spatial characteristics of compound flooding may shift over
564 time due to anthropogenically-induced changes to geometry.

5- Author contribution

566 Ramin Familkhalili: Methodology, Software, Validation, Formal analysis, Investigation, Data
567 Curation, Writing - Original Draft, Writing - Review & Editing, Visualization

568 Stefan Talke: Conceptualization, Methodology, Formal Analysis, Resources, Writing - Review &
569 Editing, Supervision, Project administration, Funding acquisition.

570 David Jay: Conceptualization, Methodology, Formal Analysis, Resources, Writing - Review &
571 Editing, Supervision.

6- Competing interests

573 The authors declare that they have no conflict of interest.

7- Data availability

575 The data used are listed within the body of the manuscript and references.

8- Acknowledgements

577 Funding was provided by the US Army Corps of Engineers (award W1927N-14-2-0015) and the
578 National Science Foundation (awards 1455350 and 1854946).

9- References

Bilskie, M. V. and Hagen, S. C.: Defining Flood Zone Transitions in Low-Gradient Coastal Regions, Geophys. Res. Lett., 45, 2761–2770, https://doi.org/10.1002/2018GL077524, 2018.

Buschman, F. A., Hoitink, A. J. F., Van Der Vegt, M., & Hoekstra, P. (2009). Subtidal water level variation controlled by river flow and tides. Water Resources Research, 45, W10420. https://doi.org/10.1029/2009WR008167

Cai, H., H. H. G. Savenije, and M. Toffolon (2014), Linking the river to the estuary: influence of river discharge on tidal damping, Hydrol. Earth Syst. Sci., 18(1), 287–304, doi:10.5194/hess-18-287-2014.

Dronkers, J. J. (1964), Tidal Computations in Rivers and Coastal Waters, North-Holland, New York, 296–304.

Familkhalili, R., and Talke, S. A. (2016), The effect of channel deepening on tides and storm surge: A case study of Wilmington, NC, Geophys. Res. Lett., 43, 9138– 9147, doi:10.1002/2016GL069494.

Familkhalili, R., Talke, S. A., & Jay, D. A. (2020). Tide-storm surge interactions in highly altered estuaries: How channel deepening increases surge vulnerability. Journal of Geophysical Research: Oceans, 125, e2019JC015286. https://doi.org/10.1029/2019JC015286

Friedrichs, C. T., and Aubrey, D. G. (1994), Tidal propagation in strongly convergent channels. Journal of Geophysical Research, 99(C2), 3321–3336. http://doi.org/10.1029/93JC03219

Giese, B. S., and D. A. Jay (1989), Modeling tidal energetics of the Columbia River estuary, Estuarine Coastal Shelf Sci., 29(6), 549–571, doi:10.1016/02727714(89)90010-3

Godin, G. (1985), Modification of rivertides by the discharge, J. Waterway, Port, Coastal, Ocean Eng., 1985, 111(2): 257-274

Godin, G. (1991), Compact approximations to the bottom friction term for the study of tides propagating in channels. Continental Shelf Research 11 (7), 579–589

Godin, G. (1999), The propagation of tides up rivers with special considerations on the upper Saint Lawrence River, Estuarine, Coastal and Shelf Science, 48, 307 – 324.

Godin, G., Martinez, A., (1994): Numerical experiments to investigate the effects of quadratic friction on the propagation of tides in a channel, Continental Shelf Research, Vol. 14, No. 7/8, pp. 723-748, 1994

Helaire, L. T., Talke, S. A., Jay, D. A., & Mahedy, D. (2019). Historical changes in Lower Columbia River and estuary floods: A numerical study. Journal of Geophysical Research: Oceans, 124, 7926–7946. https://doi.org/10.1029/ 2019JC015055.

Helaire, L. T., Talke, S. A., Jay, D. A., & Chang, H. (2020). Present and Future Flood Hazard in the Lower Columbia River Estuary: Changing Flood Hazards in the Portland-Vancouver Metropolitan Area. Journal of Geophysical Research: Oceans, https://doi.org/10.1029/2019JC015928

Horrevoets, A., H. Savenije, J. Schuurman, and S. Graas (2004), The influence of river discharge on tidal damping in alluvial estuaries, J. Hydrol., 294(4), 213–228.

Hoitink, A. J. F., and D. A. Jay (2016), Tidal river dynamics: Implications for deltas, Rev. Geophys., 54, 240–272, doi:10.1002/2015RG000507.

Jay, D. A. (1991). Green's law revisited: Tidal long-wave propagation in channels with strong topography. Journal of Geophysical Research, 96(C11), 20585. http://doi.org/10.1029/91JC01633

624 Jay, D. A. and E. P. Flinchem (1997), Interaction of fluctuating river flow with a barotropic tide:
625   A test of wavelet tidal analysis methods, J. Geophys. Res. 102:5705 – 5720.
626 Jay, D. A., K. Leffler and S. Degens (2011), Long-term evolution of Columbia River tides, ASCE
627   Journal of Waterway, Port, Coastal, and Ocean Engineering, 137: 182-191; doi:
628   10.1061/(ASCE)WW.1943- 5460.0000082.
629 Jay, DA, A. Devlin, D. Idier, E. Prococki, and RE Flick, (2021), Tides and Geomorphology: Time
630   Scales and Non-Stationary Processes, Coastal and Submarine Geomorphology, Treatise on
631   Geomorphology, https://doi.org/10.1016/B978-0-12-818234-5.00166-8
632 Johnson, F., White, C.J., van Dijk, A. et al. Natural hazards in Australia: floods. Climatic Change
633   139, 21–35 (2016). https://doi.org/10.1007/s10584-016-1689-y.
634 Jongman B, Ward PJ, Aerts JCJH. Global exposure to river and coastal flooding: Long term trends
635   and changes. Global Environmental Change 2012; 22(4): 823-35
636 Kästner, K., Hoitink, A. J. F., Torfs, P. J. J. F., Deleersnijder, E., & Ningsih, N. S. (2019).
637   Propagation of tides along a river with a sloping bed. Journal of Fluid Mechanics, 872, 39–
638   73. https://doi.org/10.1017/jfm.2019.331
639 Kukulka, T. & D.A. Jay, (2003a). Impacts of Columbia River discharge on salmonid habitat: 1. A
640   nonstationary fluvial tidal model. Journal of Geophysical Research v108 No. C9,
641   doi:10.1029/2002JC001382
642 Kukulka, T. & D.A. Jay, (2003b). Impacts of Columbia River discharge on salmonid habitat: 2.
643   Changes in shallow-water habitat. Journal of Geophysical Research v108 No. C9,
644   doi:10.1029/2002JC001829
645 Lanzoni, S., and G. Seminara, On tide propagation in convergent estuaries, J. Geophys. Res., 103,
646   30,793–30,812, 1998
647 Munchow, A. K., Masse, A. K. & Garvine, R. W. 1992 Astronomical and nonlinear tidal currents
648   in a coupled estuary shelf system. Continental Shelf Research 12, 471-498.
649 Nicholls, R.J., P.P. Wong, V.R. Burkett, J.O. Codignotto, J.E. Hay, R.F. McLean, S. Ragoonaden
650   and C.D. Woodroffe, 2007: Coastal systems and low-lying areas. Climate Change 2007:
651   Impacts, Adaptation and Vulnerability. Contribution of Working Group II to the Fourth
652   Assessment Report of the Intergovernmental Panel on Climate Change, M.L. Parry, O.F.
653   Canziani, J.P. Palutikof, P.J. van der Linden and C.E. Hanson, Eds., Cambridge University
654   Press, Cambridge, UK, 315-356.
655 Nicholls RJ, Hoozemans FMJ, Marchand M. 1999. Increasing flood risk and wetland losses due
656   to global sea-level rise: regional and global analyses. *Glob. Environ. Change* 9: S69–87
657 Olsen Associates Inc. (2012), Calibration of a Delft3D model for Bald Head Island and the Cape
658   Fear River entrance phase 1, 6114(April).
659 Orton, P., Georgas, N., Blumberg, A., and Pullen, J. (2012), Detailed modeling of recent severe
660   storm tides in estuaries of the New York City region, J. Geophys. Res., 117, C09030,
661   doi:10.1029/2012JC008220.
662 Orton, P., Talke, S., Jay, D., Yin, L., Blumberg, A., Georgas, N., Zhao, H., Roberts, H.,
663   MacManus, K. (2015). Channel Shallowing as Mitigation of Coastal Flooding. Journal of
664   Marine Science and Engineering, 3(3), 654–673. http://doi.org/10.3390/jmse3030654
665 Orton, P. M., T. M. Hall, S. Talke, A. F. Blumberg, N. Georgas, and S. Vinogradov, 2016: A
666   validated tropical-extratropical flood hazard assessment for New York Harbor. J. Geophys.
667   Res. Oceans, 121, 8904–8929, doi:https://doi.org/10.1002/2016JC011679

668   Parker, B. B., 1991. The relative importance of the various nonlinear mechanisms in a wide range
669   of tidal interactions. In: Progress in Tidal Hydrodynamics, Ed. by B. B. Parker, JohnWiley,
670   pp. 237-268.
671   Prandle, D., and Rahman, M. (1980). Tidal response in estuaries. Journal of Physical
672   Oceanography, 10(10), 1552–1573.
673   Ralston, D. K., Warner, J. C., Geyer, W. R., and Wall, G. R. (2013), Sediment transport due to
674   extreme events: The Hudson River estuary after tropical storms Irene and Lee, Geophys.
675   Res. Lett., 40, 5451– 5455, doi:10.1002/2013GL057906.
676   Ralston, D. K., Talke, S., Geyer, W. R., Al-Zubaidi, H. A. M., & Sommerfield, C. K. (2019).
677   Bigger tides, less flooding: Effects of dredging on barotropic dynamics in a highly modified
678   estuary. Journal of Geophysical Research: Oceans,124, 196–211.
679   https://doi.org/10.1029/2018JC014313
680   Savenije, H. H. G. (1998), Analytical expression for tidal damping in alluvial estuaries, J Hydraul
681   Eng-Asce, 124(6), 615–618.
682   Savenije, H. H. G., M. Toffolon, J. Haas, and E. J. M. Veling (2008), Analytical description of
683   tidal dynamics in convergent estuaries, J. Geophys. Res.,113, C10025,
684   doi:10.1029/2007JC004408.
685   Talke, S. A., P. Orton, and D. A. Jay (2014), Increasing storm tides in New York Harbor, 1844–
686   2013, Geophys. Res. Lett., 41, 3149–3155, doi:10.1002/2014GL059574.
687   Talke, S. A., Familkhalili, R., & Jay, D. A. (2021). The influence of channel deepening on tides,
688   river discharge effects, and storm surge. Journal of Geophysical Research: Oceans, 126,
689   e2020JC016328. https://doi.org/10.1029/2020JC016328
690   Talke, S.A and D.A. Jay (2020). Changing tides: The role of natural and anthropogenic factors.
691   Annual Review of Marine Science, https://doi.org/10.1146/annurev-marine-010419-010727
692   Toffolon, M., and H. H. Savenije (2011), Revisiting linearized one-dimensional tidal propagation,
693   J. Geophys. Res.,116, C07007,doi:10.1029/2010JC006616.
694   van Oldenborgh, G. J., van der Wiel, K., Sebastian, A., Singh, R., Arrighi, J., Otto, F., et al. (2017).
695   Attribution of extreme rainfall from Hurricane Harvey, August 2017. Environmental
696   Research Letters,12, 124009
697   Wahl, T., S. Jain, J. Bender, S. D. Meyers, and M. E. Luther (2015), Increasing risk of compound
698   flooding from storm surge and rainfall for major US cities, Nat. Clim. Change,5(12), 1093–
699   1097, doi:10.1038/NCLIMATE2736.
700   Wang, S.-Y. S., Zhao, L., Yoon, J.-H., Klotzbach, P., & Gillies, R. R. (2018). Attribution of climate
701   effects on Hurricane Harvey's extreme rainfall in Texas. Environmental Research Letters,
702   13. https://doi.org/10.1088/1748-9326/aabb85.
703   Winterwerp JC, Wang ZB, van Braeckel A, van Holland G, Kösters F. 2013. Man-induced regime
704   shifts in small estuaries—II: a comparison of rivers. Ocean Dyn. 63:1293–306
705   Wong, P. P., I. J. Losada, J.-P. Gattuso, J. Hinkel, A. Khattabi, K. L. McInnes, Y. Saito, and A.
706   Sallenger (2014), Coastal systems and low-lying areas, in Climate Change 2014: Impacts,
707   Adaptation, and Vulnerability, Part A: Global and Sectoral Aspects, Contribution of
708   Working Group II to the Fifth Assessment Report of the Intergovernmental Panel on Climate
709   Change, edited by C. B. Field et al., pp. 361–409, Cambridge Univ. Press, Cambridge, U. K.
710   Zheng, F.; Westra, S.; Leonard, M.; Sisson, S.A. Modeling dependence between extreme rainfall
711   and storm surge to estimate coastal flooding risk. Water Resour. Res. 2014, 50, 2050–2071.
712   Zscheischler, J., Westra, S., van den Hurk, B.J.J.M. et al. Future climate risk from compound
713   events. Nature Clim Change 8, 469–477 (2018). https://doi.org/10.1038/s41558-018-0156-3